Journal of Power Sources 196 (2011) 6048–6054

Contents lists available at ScienceDirect

Journal of Power Sources

journal homepage: www.elsevier.com/locate/jpowsour

Effects of crystal Structure of yttria- and scandia-stabilized zirconia in nickel-based SOFC anodes on carbon deposition and oxidation behavior

Hirofumi Sumi, Pramote Puengjinda, Hiroki Muroyama, Toshiaki Matsui, Koichi Eguchi*

Department of Energy and Hydrocarbon Chemistry, Graduate School of Engineering, Kyoto University, Nishikyo-ku, Kyoto 6158510, Japan

ARTICLE INFO

Article history:
Received 22 February 2011
Received in revised form 22 March 2011
Accepted 29 March 2011
Available online 6 April 2011

Keywords:
Solid oxide fuel cell (SOFC)
Internal reforming
Carbon deposition
Raman spectroscopy
Temperature programmed oxidation

ABSTRACT

The effect of crystal structure of yttria- (YSZ) and scandia-stabilized zirconia (ScSZ) in nickel-based SOFC anodes was investigated in relation with carbon deposition and oxidation behavior in methane fuel. The lattice parameter of the zirconia decreased by the dissolution of 1–2 mol%Ni to YSZ and ScSZ. For Ni-doped ScSZ, the lattice parameter of the zirconia increased by the Ni dissolution, and the crystal structure of the zirconia was modified after reduction treatment. New finer Ni particles were formed around original Ni grains accompanied by the decrease in Ni solubility to ScSZ after reduction treatment. Carbon deposition was initiated near the boundary between Ni particles and YSZ (or ScSZ) substrate in dry methane atmosphere. Furthermore, the rod-shaped carbon was observed to grow from the new finer Ni particles on the ScSZ substrate. On the other hand, a large amount of amorphous carbon was promoted to be deposited on Ni-YSZ cermet at a high temperature of 1273 K. The amorphous carbon, however, was oxidized at lower temperatures than graphite. The carbon deposition and oxidation behavior was strongly affected by the morphology and crystallinity of deposited carbon.

1. Introduction

Solid oxide fuel cells (SOFCs) are power sources with high energy conversion efficiency. Power generation by direct supply of hydrocarbon is possible for SOFCs through the internal reforming for hydrocarbon fuel, because of their high temperature operation around 1073 – 1273 K. However, solid carbon can be easily deposited on the anode due to direct supply of hydrocarbon at high temperatures, and it causes the electrode deterioration. For methane fuel, no carbon is deposited under internal and/or external steam reforming at 1073 – 1273 K and $H_2O/CH_4 \geq 1$ in the thermodynamic equilibrium [1,2]. The H_2O/CH_4 ratio possibly decreases, when gas flow and steamer systems is broken down. Therefore, fuel electrode with high durability against carbon deposition is desired to be developed. For instance, Cu-based and Ru-doped anodes are reported to have high tolerance to carbon deposition [3–7]. However, the Cu-based anodes have less activity for reforming, and the Ru-doped anodes are more expensive than conventional Ni-based anodes.

It was previously reported that the dopant into zirconia affected the electrode performance and durability in the Ni-based anodes [8,9]. Ni-scandia stabilized zirconia (ScSZ) anode was less suffered from carbon deposition than Ni-yttria stabilized zirconia (YSZ) anode under power generation by internal reforming of methane at low H_2O/CH_4 ratios and at 1273 K. While fibrous and rod-shaped graphite was observed on the Ni-ScSZ anode after power generation, a large amount of amorphous carbon was deposited on the Ni-YSZ anode. Several studies have also reported that the ratio of amorphous carbon and crystalline graphite depended on the oxide species such as YSZ, ScSZ, Sm-doped ceria and $(La,Sr)(Ga,Mn)O_3$ in SOFC anodes [10–12]. Furthermore, the carbon deposition behavior depended on the operating temperature [9,13,14]. The rate of carbon deposition for the Ni-YSZ anode was faster than that for the Ni-ScSZ anode at 1273 K, whereas the order was opposite at 1123 K. However, the reason for the selectivity of oxide species and the effect of operating temperature has not been clarified so far.

Cubic zirconia phase is generally stabilized by doping yttria and scandia for SOFC electrolytes [15,16]. The crystal structure of YSZ and ScSZ was previously evaluated by X-ray diffraction and Raman spectroscopy [17–22]. The ScSZ phase was reported to be more sensitive to the treatment condition than YSZ phase. Matsui et al. reported that the ScSZ phase was affected by the heat treatment temperature [20]. Kishimoto et al. and Puengjinda et al. have reported that the ScSZ phase was changed from cubic to rhombohedral during reduction–oxidation (redox) treatment [21,22] Moreover, the cubic phase of the zirconia is stabilized by dissolution of a small amount of nickel into zirconia [23–25]. The difference in the stability of zirconia phase is likely to affect the change of the carbon deposition behavior for Ni-based SOFC anodes.

Catalytic properties of SOFC anode materials were evaluated by several studies. The interaction between nickel and zirconia was confirmed to become strong with increasing Ni content for Ni-

* Corresponding author. Tel.: +81 0 75 383 2519; fax: +81 0 75 383 2520.
E-mail address: eguchi@scl.kyoto-u.ac.jp (K. Eguchi).

0378-7753/$ – see front matter © 2011 Elsevier B.V. All rights reserved.
doi:10.1016/j.jpowsour.2011.03.092

YSZ and Ni-ScSZ cermets by temperature programmed reduction (TPR) technique [26,27]. The interaction between nickel and ScSZ was stronger than that between YSZ, which is likely to affect the carbon deposition and oxidation behavior [27]. The carbon oxidation behavior could be evaluated by the temperature programmed oxidation (TPO) technique [28–30]. Carbon deposited after exposure in hydrocarbon was combusted at several temperature regions on Ni-YSZ cermet. This suggests the existence of several carbon species. Pomfret et al. [31,32] conducted in situ observation of Raman spectra under open circuit voltage and current loading states with supplies of hydrocarbons for Ni-YSZ|YSZ|(La,Sr)MnO_3 cells due to examine the crystalline graphite deposition and electrochemical oxidation behaviors. However, amorphous carbon more affects the short-term deterioration than graphite for SOFC anodes [8,9]. Therefore, it is important to investigate the deposition and oxidation behaviors for the carbon species such as carbon fiber, amorphous carbon and graphite.

In this study, the effect of redox treatment was evaluated in relation with the crystal structure and nickel dissolution for YSZ and ScSZ with X-ray diffraction and Raman spectroscopy in consideration of cell manufacturing and power generation conditions. The shape changes of nickel particles and deposited carbon on YSZ and ScSZ disks were also observed after redox treatment and methane exposure with field emission-scanning electron microscopy (FE-SEM). Furthermore, the carbon species deposited at different temperatures in methane was examined for Ni-YSZ and Ni-ScSZ cermets. The carbon species were evaluated by electrochemical oxidation during power generation test as well as by TPO technique.

2. Experimental

2.1. Evaluation of crystal structure for YSZ and ScSZ

In this study, commercial YSZ ($(Y_2O_3)_{0.08}$–$(ZrO_2)_{0.92}$; Tosoh Corp.) and ScSZ ($(Sc_2O_3)_{0.1}$–$(CeO_2)_{0.01}$–$(ZrO_2)_{0.89}$); Daiichi Kigenso Kagaku Kogyo Co., Ltd.) powders were used. The NiO (Wako Pure Chemical Industries, Ltd.) and YSZ (or ScSZ) powders were mixed in ethanol for 24 h. The dried x mol%Ni-Y(Sc)SZ powders (x = 0–5) were calcined at 1673 K for 5 h in air. The crystal structure was evaluated with X-ray diffraction (Rigaku Ultima IV; 2θ = 20–140°) and Raman spectroscopy (Horiba Jobin Yvon LabRAM HR-800; 441.6 nm He–Cd laser). Then, the powers were calcined at 1073 K for 2 h in 10%H_2–N_2 mixture, and the similar series of experiments were conducted.

2.2. Observation of nickel particles and deposited carbon

The YSZ and ScSZ powders were uniaxially shaped into disks, and cold-isostatically pressed at 180 MPa. The disks were calcined at 1773 K for 10 h in air. Nickel thin-film was formed by radio frequency sputtering (Showa Shinku SPH-04H; power 60 W for 30 min) in 2.67 Pa of Ar atmosphere on the YSZ (or ScSZ) surface which was buffed with diamond compound (0.25 μm). The thickness of nickel thin-film was ca. 50 nm. After Ni sputtering, the YSZ and ScSZ disks were calcined at 873 K for 5 h in 10%H_2–N_2 mixture to change from Ni thin-film to particles. The morphological change of nickel particles was observed with FE-SEM (Carl Zeiss NVision40; accelerating voltage 1.5 kV) after calcinations at 873 K for 5 h in air and 10%H_2–N_2 mixture as oxidation and re-reduction treatment, respectively. Then, the YSZ and ScSZ disks after exposure to 10%CH_4–N_2 mixture at 1073 K for 10 and 60 min were observed with FE-SEM to investigate the carbon deposition behavior.

2.3. Evaluation of carbon deposition and oxidation behaviors

The NiO and YSZ (or ScSZ) powders were mixed in ethanol for 24 h. The volume ratio of Ni to zirconia was 50: 50 after nickel reduction. The mixed powders were calcined at 1573 K for 5 h in air. The powders were pressed, crushed, and sieved to a particle size of 0.85–1.7 mm. The carbon species were evaluated with Raman spectroscopy for the Ni-YSZ and Ni-ScSZ cermets after exposure to 10%H_2–N_2 mixture for 2 h at 1073 and 1273 K, and 10%CH_4–N_2 mixture for 1 h. Then, the productions of CO and CO_2 were measured with mass spectroscopy (Anelva M-200QA-M) during TPO from room temperature to 1273 K at 10 K/min in 5%O_2–He mixture. To evaluate the electrochemical oxidation of deposited carbon, the coin-shaped SOFCs were manufactured. The electrolyte, anode and cathode were YSZ (thickness 500 μm), Ni-Y(Sc)SZ (sintering temperature 1573 K) and $(La_{0.8}Sr_{0.2})_{0.98}MnO_{3+\delta}$ (AGC Seimi Chemical CO., Ltd.; sintering temperature 1423 K), respectively. The thickness and diameter of the electrodes were 30 μm and 6 mm, respectively. The Ni-Y(Sc)SZ anodes were observed with Raman spectroscopy after exposure to 10%CH_4–N_2 mixture without current loading at 1273 K for 1 h, and then with current loading at 0.3 A/cm^2 for 1 h in the same atmosphere.

3. Results and discussion

3.1. Evaluation of crystal structure for YSZ and ScSZ

The crystal structure of x mol%Ni-Y(Sc)SZ powders (x = 0–5) were evaluated with X-ray diffraction after air calcination and reduction treatments. The X-ray diffraction peaks were attributed to cubic zirconia for the all samples. Peak from monoclinic, tetragonal and rhombohedral zirconia was not observed. Fig. 1 shows the lattice parameter for (a) Ni-doped YSZ and (b) Ni-doped ScSZ as a function of Ni content after calcination at 1673 K in air and at 1073 K in H_2/N_2. The lattice parameter of the zirconia decreased by doping of nickel for both of YSZ and ScSZ. Kuzjukevisc and Linderoth also reported the decrease in lattice parameter by nickel doping to YSZ [23]. These results suggest the occurrence of solid dissolution of Ni^{2+} ion with its radius is smaller than Zr^{4+} ion. The nickel solubility is 1–2 mol% for YSZ and ScSZ, because the lattice parameter was unchanged above 2 mol%Ni. The lattice parameter of the zirconia was unchanged for oxidized and reduced YSZ with and without nickel. However, the lattice parameter for oxidized ScSZ without nickel was larger than that for reduced one. The rhombohedral zirconia was reported to have larger lattice parameter than the cubic zirconia [18]. Although the rhombohedral zirconia was not detected by X-ray diffraction, the small amount of rhombohedral phase was possibly included in ScSZ. On the other hand, the lattice parameter increased after reduction treatment for the Ni-doped ScSZ, which suggests the decrease in nickel solubility.

Previously, the crystal structure of YSZ and ScSZ was also evaluated with Raman spectroscopy [17–19,21]. However, the effects of nickel doping and redox treatment were not investigated precisely in relation with the crystal structure of the zirconia. Fig. 2 shows the Raman spectra for (a) Ni-doped YSZ and (b) Ni-doped ScSZ after calcination at 1673 K in air and at 1073 K in H_2/N_2. The peak at ca. 620 cm^{-1} appeared for the all conditions, which was attributed to cubic zirconia. On the other hand, the appearance of the peak at ca. 480 cm^{-1} suggests the existence of the other phase than the cubic zirconia. The peak at ca. 480 cm^{-1} for YSZ was smaller than that for ScSZ, which supported the amount of monoclinic, tetragonal and rhombohedral zirconia was little for YSZ. The spectra for YSZ were unchanged by nickel doping and redox treatment since no phase transition proceeded with these treatments. The intensity of this peak weakened by nickel doping to ScSZ. Fur-

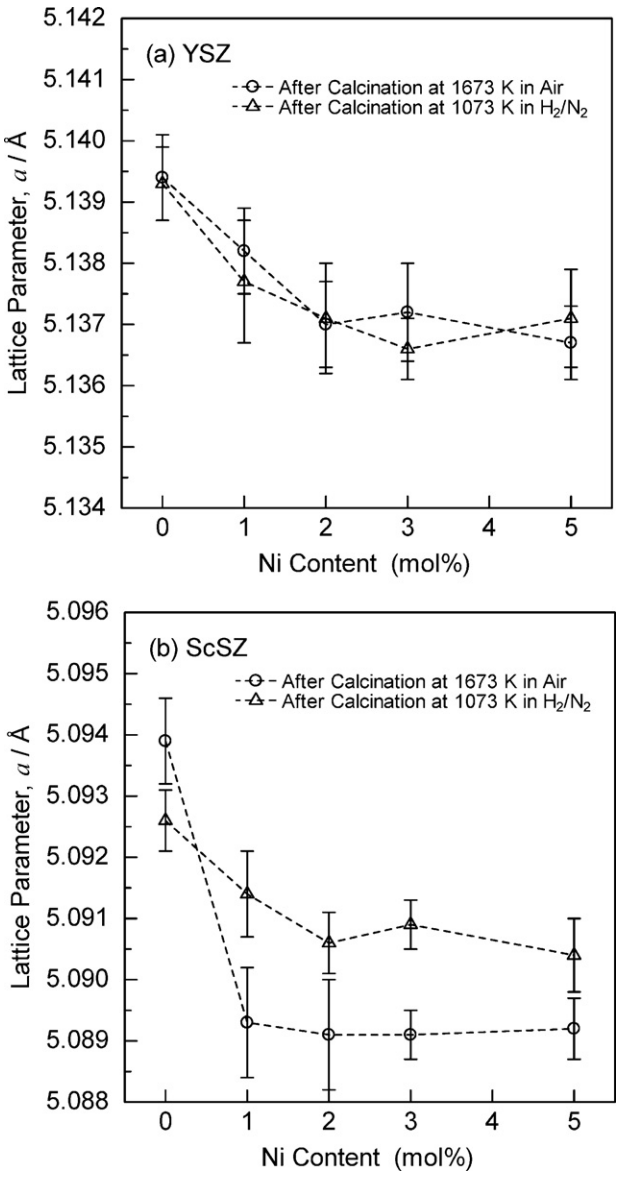

Fig. 1. Lattice parameters for (a) Ni-doped YSZ and (b) ScSZ after calcination at 1673 K in air and at 1073 K in H_2/N_2.

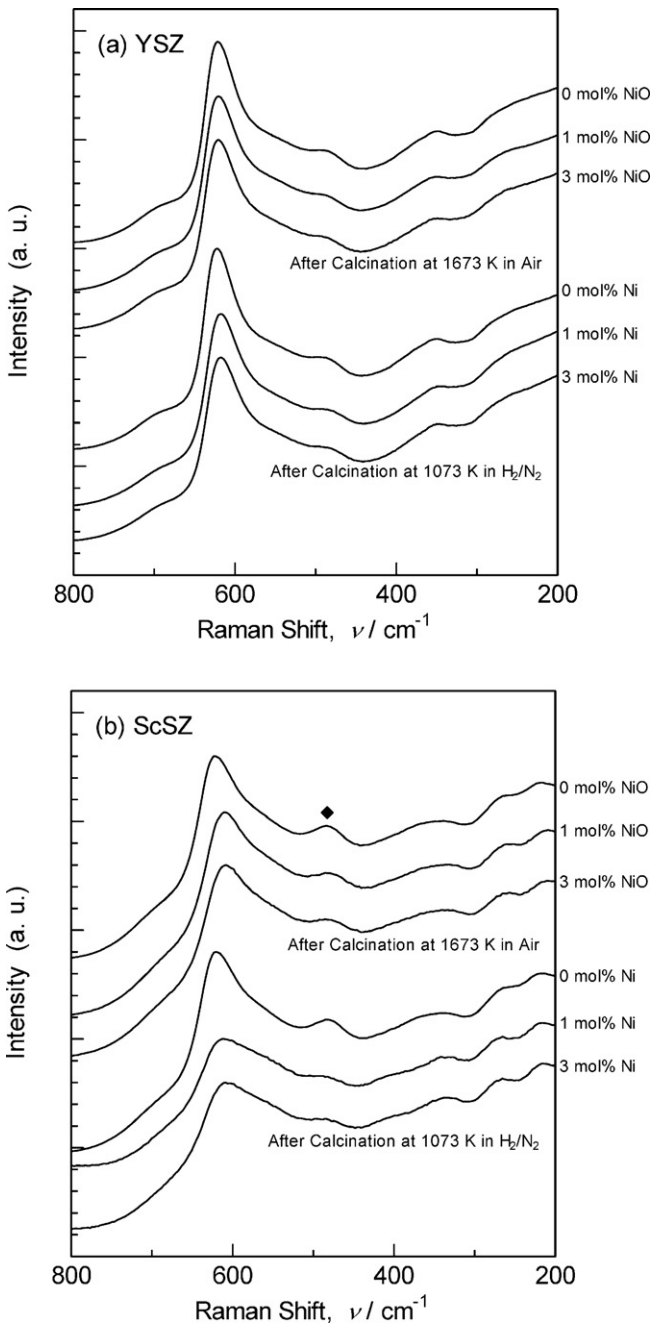

Fig. 2. Raman spectra for (a) Ni-doped YSZ and (b) ScSZ after calcination at 1673 K in air and at 1073 K in H_2/N_2.

thermore, the peak almost disappeared by reduction treatment for the 1 mol%Ni-doped ScSZ. The intensity of this peak was almost unchanged between 1 mol% and 3 mol%Ni-doped ScSZ. The crystal structure of ScSZ was slightly changed by nickel doping and redox treatment. It is concluded that the ScSZ phase is more sensitive to the nickel dissolution and redox treatment than YSZ phase.

3.2. Observation of nickel particles and deposited carbon

The YSZ and ScSZ disks with nickel sputtering were observed with FE-SEM after redox treatment. Fig. 3 shows the secondary electron images for nickel particles on (a) YSZ and (b) ScSZ disks after (i) reduction, (ii) oxidation and (iii) re-reduction treatments. After first reduction treatment, nickel was changed from thin-film to particles, and 1–2 mol%Ni was dissolved into YSZ and ScSZ as well as the result of Fig. 1. The surface of nickel particles was smooth after reduction treatment. However, the surface became rough after oxidation treatment due to conversion to nickel oxide. The similar "sponge-liked" nickel oxide was reported by several studies [33–36]. While the nickel particles returned to original shape on the YSZ disk after re-reduction treatment, finer particles were newly deposited around the original nickel grains for the ScSZ disk as represented by arrows in Fig. 3 (b-iii). This result also supports that the nickel solubility to ScSZ decreased by reduction treatment. Linderoth et al. reported that the decrease in nickel solubility was caused by the phase transition from cubic to tetragonal for 1.5 mol%Ni-YSZ after reduction treatment at 1273 K for 150 h in $2\%H_2O$–$9\%H_2$–N_2 mixture [24]. In this study, the reduction temperature and time were lower (873 K) and shorter (2 h) than their reports. Therefore, the lattice parameter and crystal phase were unchanged for Ni-doped YSZ as shown in Figs. 1(a) and 2(a). On the other hand, the crystal structure of the zirconia slightly changed by redox treatment for the Ni-doped ScSZ as shown in Fig. 2(b), which led to the change in nickel solubility.

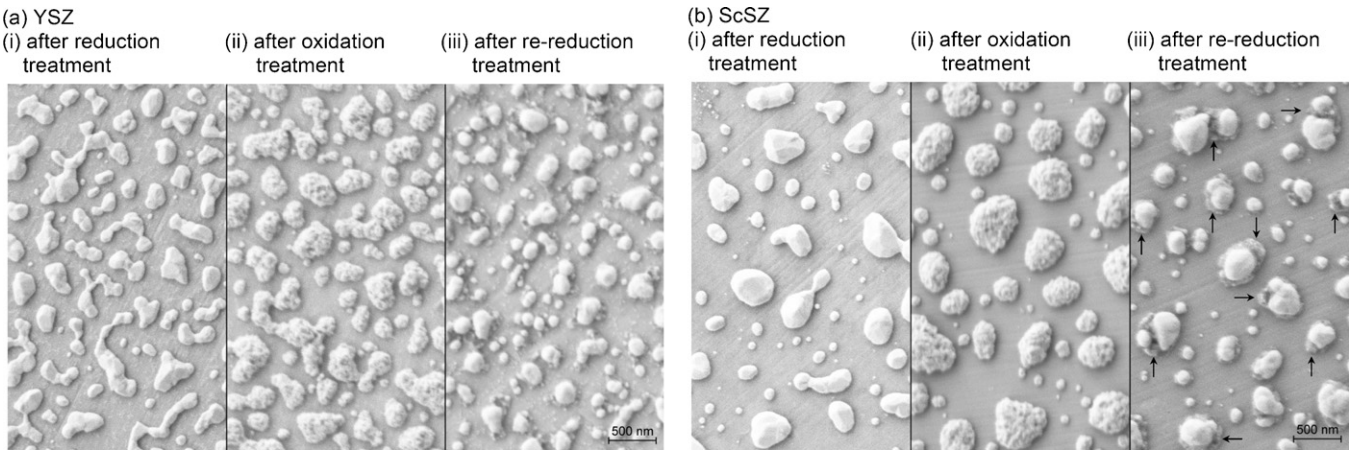

Fig. 3. Secondary electron images for nickel particles on (a) YSZ and (b) ScSZ disks after (i) reduction, (ii) oxidation and (iii) re-reduction treatments. The arrows were ascribed to fine nickel particles which were newly deposited after re-reduction treatment.

Table 1
Peak intensity ratio of D-band/G-band (I_D/I_G) for Ni-YSZ and Ni-ScSZ cermets after exposure to 10%$CH_4 - N_2$ for 1 h at 1073 K and 1273 K.

Material	Exposure temperature	I_D/I_G
Ni-YSZ	1073 K	0.137
	1273 K	0.208
Ni-ScSZ	1073 K	0.094
	1273 K	0.077

Table 2
Peak area ratio of separated TPO profiles for Ni-YSZ and Ni-ScSZ cermets after exposure to 10%$CH_4 - N_2$ for 1 h at 1073 K and 1273 K.

Exposure temperature	Ni-YSZ		Ni-ScSZ	
	1073 K	1273 K	1073 K	1273 K
C_α	0.011	0.007	0.056	0.019
C_β	0.300	0.499 + α[a]	0.344	0.539
C_γ	0.233	0.392	0.239	0.442
Total	0.544	0.897 + α[a]	0.629	1.000[b]

[a] A large amount of CO was produced.
[b] The values are normalized as the total area is unity for the Ni-ScSZ cermet exposed at 1273 K.

Carbon deposition behavior was observed using the YSZ and ScSZ disks after re-reduction treatment. Fig. 4 shows the secondary and backscattered electron images for nickel particles on (a) YSZ and (b) ScSZ disks after exposure to CH_4/N_2 mixture for (i) 10 and (ii) 60 min. The black areas in the backscattered electron images were ascribed to deposited carbon by an energy-dispersive X-ray spectrometer. Carbon was observed around nickel particles after 10 min for both on the YSZ and ScSZ disks. The similar behavior was also observed for an embedded nickel mesh on YSZ by Yashiro et al. [37]. This is caused by the strong interaction between nickel and zirconia observed by the TPR technique [26,27]. The polarization resistance increased rapidly when the fuel changed from 5%H_2O–H_2 to 5%H_2O–10%CH_4–N_2 mixtures [9]. This phenomenon was caused by the decrease in active triple phase boundaries due to carbon deposition. After exposure to CH_4/N_2 for 60 min, the whole surface of nickel particles was covered with carbon on the YSZ and ScSZ disks. Furthermore, rod-shaped carbon was also observed only on the ScSZ disk as represented by circles in Fig. 4 (b-ii). The similar carbon was also observed for Ni-ScSZ anode after power generation at 1273 K in $H_2O/CH_4 = 0.5$ [9]. The rod-shaped carbon seemed to grow from the fine nickel particles deposited around the original nickel grains as shown in Fig. 3 (b-iii). It is concluded that the shape of deposited carbon is strongly affected by the change of nickel

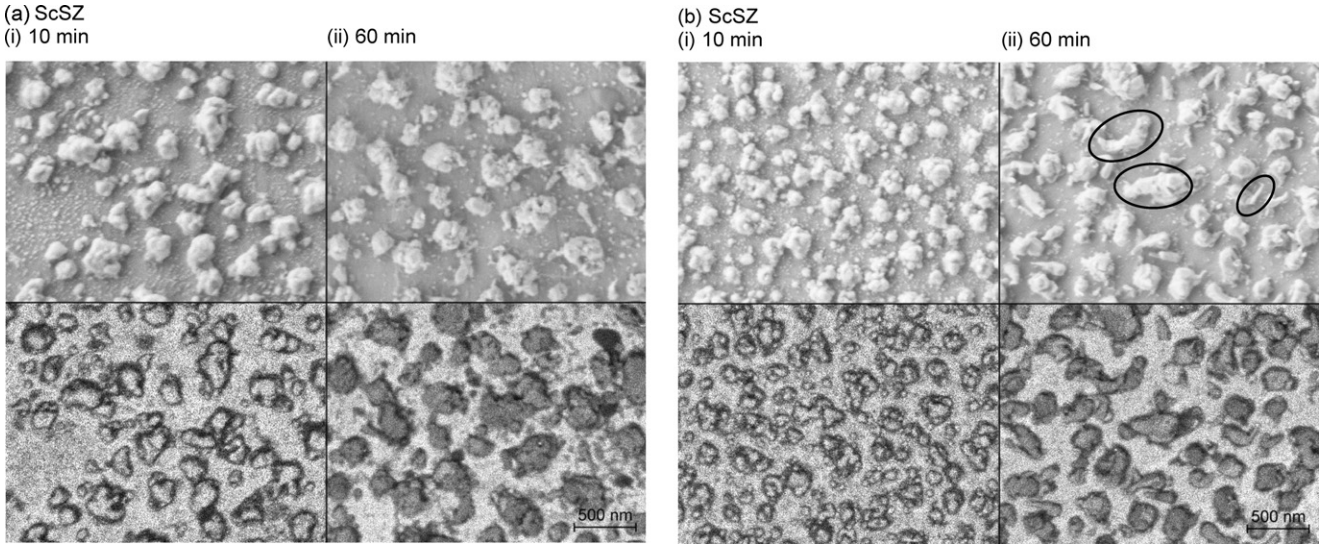

Fig. 4. Secondary electron (upper) and backscattered electron (lower) images for nickel particles on (a) YSZ and (b) ScSZ disks after exposure to CH_4/N_2 mixture for (i) 10 and (ii) 60 min. The black areas in the backscattered electron images were ascribed to deposited carbon.

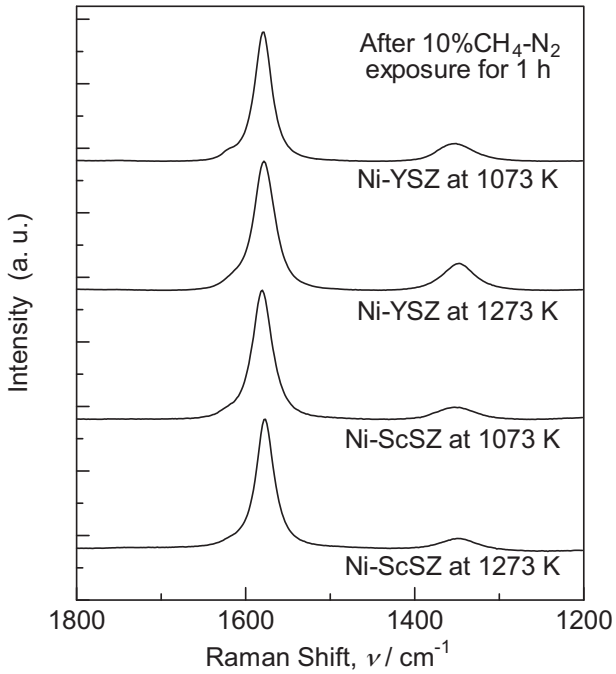

Fig. 5. Raman spectra of Ni-YSZ and Ni-ScSZ cermets after exposure to 10%CH_4–N_2 for 1 h at 1073 K and 1273 K.

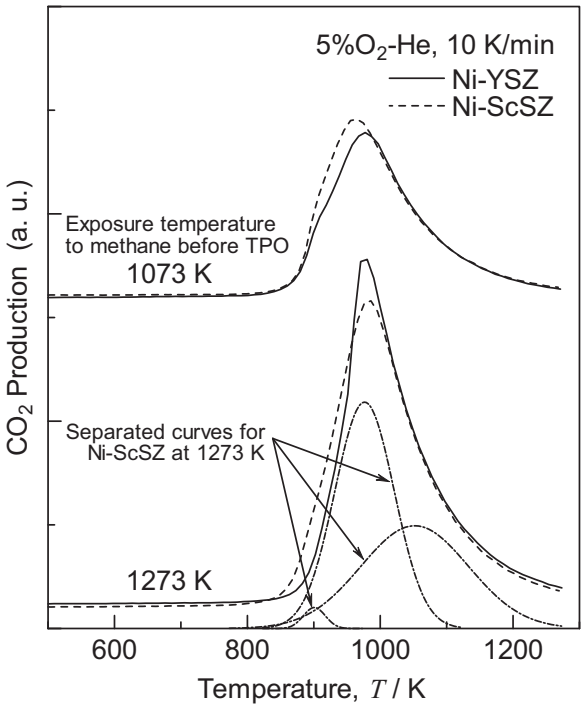

Fig. 6. CO_2 production under temperature programmed oxidation (TPO) in 5%O_2–He at a heating rate of 10 K/min for Ni-YSZ (solid line) and Ni-ScSZ (dotted line) cermets after exposure to 10%CH_4–N_2 for 1 h at 1073 K and 1273 K. Dot-dashed lines are separated into three curves for the Ni-ScSZ cermet exposed at 1273 K.

solubility to zirconia. In this experiment, the evaluation of the crystallinity of deposited carbon is difficult, because the amount of the deposited carbon was too small. The Ni-YSZ and Ni-ScSZ cermets were used to evaluate the relation between the carbon species and the deposition and oxidation behavior precisely.

3.3. Evaluation of carbon deposition and oxidation behavior

It was previously reported that the rate of carbon deposition for Ni-YSZ was larger than that for Ni-ScSZ at 1273 K, whereas the order was opposite at 1123 K [9]. This result was possibly caused by the difference in carbon species. Fig. 5 shows the Raman spectra of Ni-YSZ and Ni-ScSZ cermets after exposure to 10%CH_4–N_2 for 1 h at 1073 K and 1273 K. Two peaks were observed at 1350 cm^{-1} (D-band) and 1580 cm^{-1} (G-band), which were attributable to amorphous carbon and crystalline graphite, respectively. The spectra in Fig. 5 are normalized, so that the peak intensity of G-band is the same. The peak intensity ratios of D-band/G-band (I_D/I_G) are summarized in Table 1. The I_D/I_G ratio for the Ni-YSZ was larger than that for the Ni-ScSZ. Furthermore, the I_D/I_G ratio at 1273 K was larger than that at 1073 K for the Ni-YSZ cermet. Amorphous carbon was easily deposited at higher temperatures for the Ni-YSZ cermet by exposure to methane. The amorphous carbon was reported to

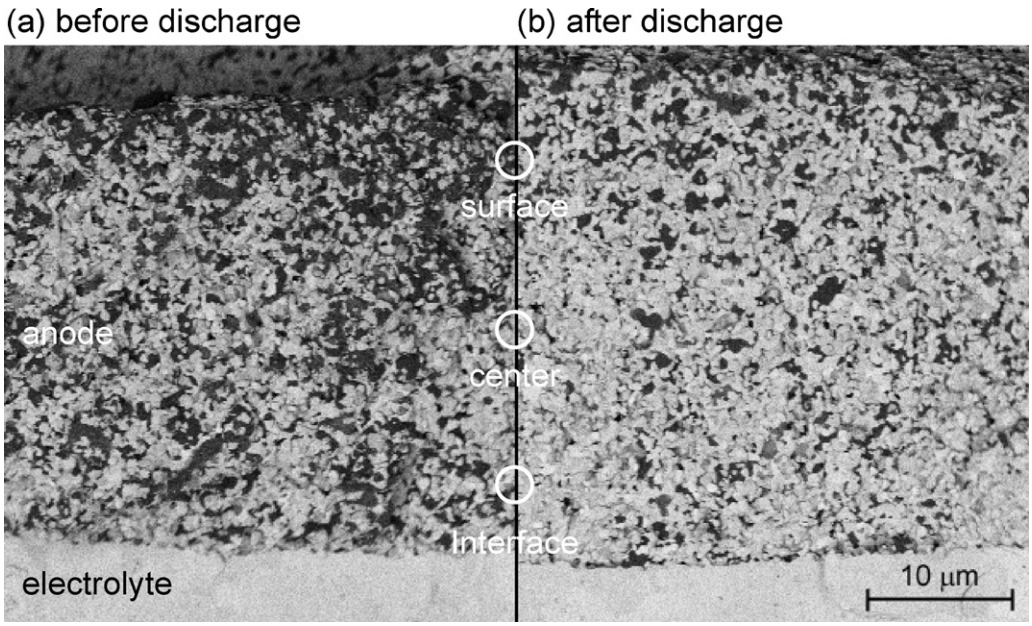

Fig. 7. Backscattered electron images of cross-section for Ni-YSZ anodes (a) before and (b) after discharge at 0.3 A/cm^2 for 1 h in 5%H_2O −10%CH_4–N_2 at 1273 K.

lead to the rapid anode deterioration [8,9]. The result in Fig. 5 supported that the durability of the Ni-YSZ anode was lower than that of Ni-ScSZ anode at low H_2O/CH_4 ratios and at 1273 K. On the other hand, the I_D/I_G ratio was small for the both of the Ni-YSZ and Ni-ScSZ cermets exposed at 1073 K, which suggests that the graphite was more easily deposited than the amorphous carbon at lower temperatures. The rate of carbon deposition for the Ni-ScSZ anode is faster than that for the Ni-YSZ anode at low temperatures as reported in the previous paper because of the high catalytic activity against methane cracking and graphite formation for the Ni-ScSZ anode. Especially, the rod-shaped graphite seemed to be formed from new fine nickel particles which were deposited by the decrease in Ni solubility to ScSZ as shown in Fig. 4 (b-ii).

Fig. 6 shows the CO_2 production under temperature programmed oxidation (TPO) in 5%O_2–He at a heating rate of 10 K/min for Ni-YSZ and Ni-ScSZ cermets after exposure to 10%$CH_4 - N_2$ for 1 h at 1073 K and 1273 K. The peaks were asymmetric with a shoulder at ca. 900 K in the TPO profiles. It has been known that carbon fiber (C_α), amorphous carbon (C_β) and crystalline graphite (C_γ) are subsequently oxidized in turn from lower temperature for Ni-based catalysts [38]. Dot-dashed lines are separated into three curves for the Ni-ScSZ cermet exposed at 1273 K. Table 2 shows the peak area ratio of separated TPO profiles. The values of Table 2 are normalized, as the total area is unity for the Ni-ScSZ cermet exposed at 1273 K. The area of the peak at the lowest temperature was large for the Ni-ScSZ cermet exposed at 1073 K, for which the large amount of fibrous and rod-shaped carbon was observed with FE-SEM. Therefore, the carbon fiber was combusted more easily than the other carbon species. The peak at the middle temperature was strong for the Ni-YSZ and Ni-ScSZ cermets exposed at a high temperature of 1273 K. Furthermore, a large amount of carbon monoxide was confirmed to be produced only for the Ni-YSZ cermet exposed at 1273 K by mass spectroscopy, because a part of deposited carbon was combusted incompletely. The total production of CO and CO_2 was large for the Ni-YSZ cermet exposed at 1273 K, which corresponds to the oxidation of amorphous carbon. The peak at the highest temperature was caused by the combustion of crystalline graphite. This order of carbon oxidation is the same as the other Ni-based catalysts [38]. Although the graphite can be formed at low temperature as shown in Fig. 5, the graphite is oxidized difficultly as a result of TPO. Therefore, the graphite has a tendency to accumulate under internal reforming for SOFCs. On the other hand, the amorphous carbon is expected to be removed by the electrochemical oxidation, because this carbon can be combusted at lower temperature than the graphite.

The carbon oxidation behavior was evaluated under current loading with internal reforming of methane for coin-shaped SOFCs. Fig. 7 shows the backscattered electron images of cross-section for Ni-YSZ anode before and after discharge at 0.3 A/cm^2 for 1 h in 5%H_2O–10%CH_4–N_2 at 1273 K. The black areas were ascribed to the deposited carbon. A large amount of deposited carbon was observed from the anode surface to the anode/electrolyte interface for Ni-YSZ anode before discharge, which was exposed to 10%CH_4–N_2 mixture for 1 h at 1273 K. After discharge, the amount of deposited carbon decreased. Especially, the electrochemical oxidation of deposited carbon was promoted near the anode/electrolyte interface. Fig. 8 shows the Raman spectra for (a) Ni-YSZ and (b) Ni-ScSZ anodes at the vicinity of surface, center and interface as shown in Fig. 7. The spectra in Fig. 8 are normalized, so that the peak intensity of G-band is the same. Before discharge, a larger amount of amorphous carbon was deposited on the Ni-YSZ anode than on the Ni-ScSZ anode, which agreed with the result in Fig. 5. The I_D/I_G ratios were almost the same from the anode surface to the anode/electrolyte interface before discharge. The D-band was weakened after discharge for either anode. Especially, the relative intensity of D-band near the anode/electrolyte interface was smaller than that near surface. This means that the amorphous carbon was oxidized preferentially by oxide ions supplied from electrolyte. Water gas reaction ($C + H_2O \rightarrow H_2 + CO$) is also expected to occur by steam production under discharge. The deposition of amorphous carbon caused a short-term deterioration of anode performance. However, the result of Fig. 8 suggests that the anode performance can be recovered partially by the electrochemical oxidation of amorphous carbon under a current loading.

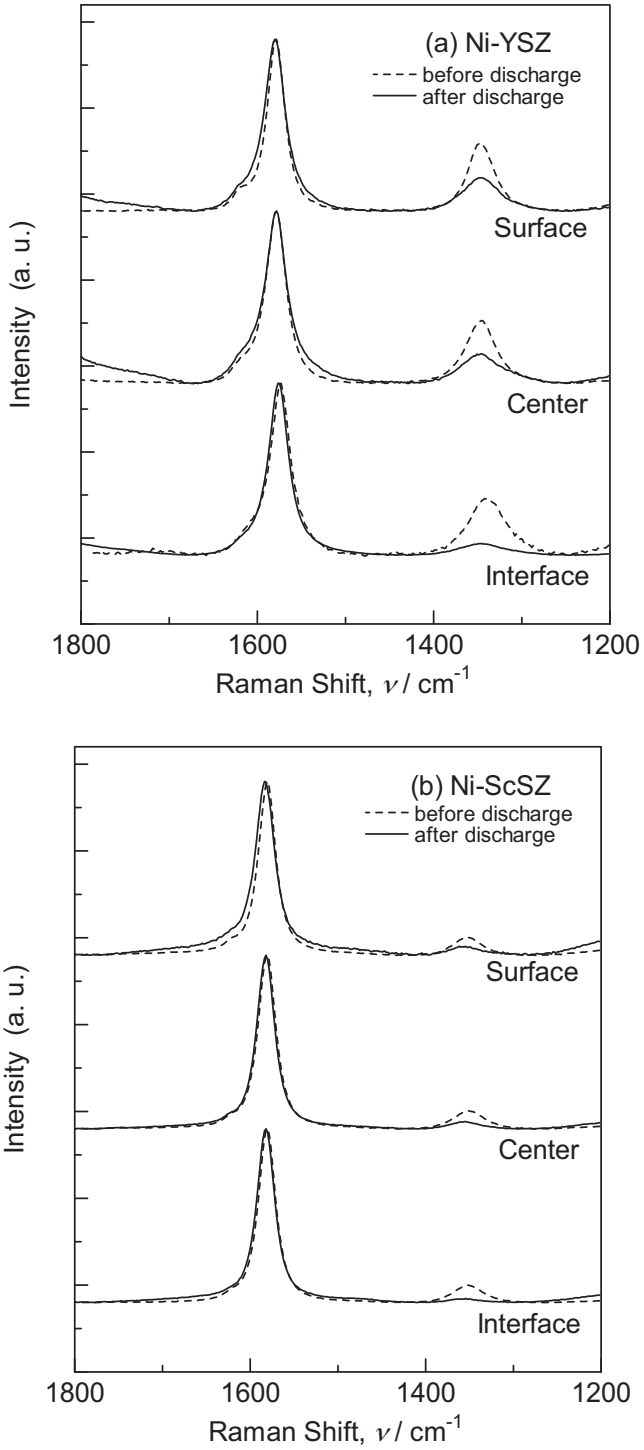

Fig. 8. Raman spectra for (a) Ni-YSZ and (b) Ni-ScSZ anodes before and after discharge at 0.3 A/cm^2 for 1 h in 5%H_2O–10%CH_4–N_2 at 1273 K.

4. Conclusion

In this study, the effect of crystal structure of YSZ and ScSZ in nickel-based SOFC anodes was investigated precisely in relation with carbon deposition and oxidation behavior in methane fuel. The lattice parameter of the zirconia decreased by the dissolution of 1–2 mol%Ni to YSZ and ScSZ. The lattice parameter and crystal structure of Ni-doped YSZ were unchanged during redox treatment. On the other hand, the lattice parameter of the zirconia increased after reduction treatment for Ni-doped ScSZ, which suggests the decrease in nickel solubility by a partial change of crystal structure. Carbon deposition was initiated near the boundary between Ni particles and YSZ (or ScSZ) substrate after exposure to methane. Furthermore, rod-shaped carbon was observed to grow from the new finer nickel particles which were deposited around the original nickel grains by reduction treatment only on the ScSZ disk. The morphology and crystallinity of the deposited carbon is strongly affected by the size of the Ni particles which are formed by the change of nickel solubility to zirconia. Amorphous carbon was easily deposited at high temperatures for Ni-YSZ cermet, which caused the rapid deterioration of anode performance. However, the amorphous carbon was combusted at lower temperature than the crystalline graphite during temperature programmed oxidation. It was also confirmed that the electrochemical oxidation of the amorphous carbon was preferential during current loading for coin-shaped SOFCs.

References

[1] K. Eguchi, H. Kojo, T. Takeguchi, R. Kikuchi, K. Sasaki, Solid State Ionics 152–153 (2002) 411–416.
[2] K. Sasaki, Y. Teraoka, J. Electrochem. Soc. 150 (2003) A878–A884.
[3] S. Park, R.J. Gorte, J.M. Vohs, J. Electrochem. Soc. 146 (1999) 3603–3605.
[4] S. Park, R.J. Gorte, J.M. Vohs, Nature 404 (2000) 265–267.
[5] R.J. Gorte, J.M. Vohs, J. Catal. 216 (2003) 477–486.
[6] T. Takeguchi, R. Kikuchi, T. Yano, K. Eguchi, K. Murata, Catal. Today 84 (2003) 217–222.
[7] T. Iida, M. Kawano, T. Matsui, R. Kikuchi, K. Eguchi, J. Electrochem. Soc. 154 (2007) B234–B241.
[8] H. Sumi, K. Ukai, Y. Mizutani, H. Mori, C.-J. Wen, H. Takahashi, O. Yamamoto, Solid State Ionics 174 (2004) 151–156.
[9] H. Sumi, Y.-H. Lee, H. Muroyama, T. Matsui, K. Eguchi, J. Electrochem. Soc. 157 (2010) B1118–B1125.
[10] T. Horita, K. Yamaji, T. Kato, N. Sakai, H. Yokokawa, J. Power Sources 131 (2004) 299–303.
[11] K. Yamaji, H. Kishimoto, Y. Xiong, T. Horita, N. Sakai, M.E. Brito, H. Yokokawa, Solid State Ionics 179 (2008) 1526–1530.
[12] M. Yoshinaga, H. Kishimoto, K. Yamaji, Y. Xiong, M.E. Brito, T. Horita, H. Yokokawa, Solid State Ionics, doi:10.1016/j.ssi.2010.05.003.
[13] A. Gunji, C.-J. Wen, J. Otomo, T. Kobayashi, K. Ukai, Y. Mizutani, H. Takahashi, J. Power Sources 131 (2004) 285–288.
[14] K. Ke, A. Gunji, H. Mori, S. Tsuchida, H. Takahashi, K. Ukai, Y. Mizutani, H. Sumi, M. Yokoyama, K. Waki, Solid State Ionics 177 (2006) 541–547.
[15] H.G. Scott, J. Mater. Sci. 10 (1975) 1527–1535.
[16] M. Hirano, S. Watanabe, E. Kato, Y. Mizutani, M. Kawai, Y. Nakamura, J. Am. Ceram. Soc. 82 (1999) 2861–2864.
[17] M. Yashima, K. Ohtake, H. Arashi, M. Kakihana, M. Yoshimura, J. Appl. Phys. 74 (1993) 7603–7605.
[18] H. Fujimori, M. Yashima, M. Kakihana, M. Yoshimura, J. Am. Ceram. Soc. 81 (1998) 2885–2893.
[19] K. Nomura, Y. Mizutani, M. Kawai, Y. Nakamura, O. Yamamoto, Solid State Ionics 132 (2000) 235–239.
[20] T. Matsui, T. Iida, R. Kikuchi, M. Kawano, T. Inagaki, K. Eguchi, J. Electrochem. Soc. 155 (2008) B1136–B1140.
[21] H. Kishimoto, N. Sakai, T. Horita, K. Yamaji, Y.-P. Xiong, M.E. Brito, H. Yokokawa, Solid State Ionics 179 (2008) 2037–2041.
[22] P. Puengjinda, H. Muroyama, T. Matsui, M. Kawano, T. Inagaki, K. Eguchi, J. Electrochem. Soc. 157 (2010) B1673–B1678.
[23] A. Kuzjukevics, S. Linderoth, Solid State Ionics 93 (1997) 255–261.
[24] S. Linderoth, N. Bonanos, K.V. Jensen, J.B. Bilde-Sørensen, J. Am. Ceram. Soc. 84 (2001) 2652–2656.
[25] H. Kondo, T. Sekino, T. Kusunose, T. Nakayama, Y. Yamamoto, K. Niihara, Mater. Lett. 57 (2003) 1624–1628.
[26] H. Mori, C.-J. Wen, J. Otomo, K. Eguchi, H. Takahashi, Appl. Catal. A 245 (2003) 79–85.
[27] K. Eguchi, K. Tanaka, T. Matsui, R. Kikuchi, Catal. Today 146 (2009) 154–159.
[28] R.T. Baker, I.S. Metcalfe, Ind. Eng. Chem. Res. 34 (1995) 1558–1565.
[29] C.M. Finnerty, N.J. Coe, R.H. Cunningham, R.M. Ormerod, Catal. Today 46 (1998) 137–145.
[30] H. He, J.M. Hill, Appl. Catal. A 317 (2007) 284–292.
[31] M.B. Pomfret, J.C. Owrutsky, R.A. Walker, Anal. Chem. 79 (2007) 2367–2372.
[32] M.B. Pomfret, J. Marda, G.S. Jackson, B.W. Eichhorn, A.M. Dean, R.A. Walker, J. Phys. Chem. C. 112 (2008) 5232–5240.
[33] D. Waldbillig, A. Wood, D.G. Ivey, J. Power Sources 145 (2005) 206–215.
[34] J. Malzbender, E. Wessel, R.W. Steinbrech, Solid State Ionics 176 (2005) 2201–2203.
[35] D. Sarantaridis, R.A. Rudkin, A. Atkinson, J. Electrochem. Soc. 155 (2008) B467–B472.
[36] T. Hatae, Y. Matsuzaki, Y. Yamazaki, Solid State Ionics 179 (2008) 274–281.
[37] K. Yashiro, M. Takase, K. Sato, T. Kawada, J. Mizusaki, ECS Trans. 16 (2008) 213–218.
[38] C.H. Bartholomew, Appl. Catal. A 212 (2001) 17–60.